EFDA–JET–PR(06)29

S. Hacquin, S. E. Sharapov, B. Alper, C. Challis, A. Fonseca, E. Mazzucato,
A. Meigs, L. Meneses, I. Nunes, S. D. Pinches and JET EFDA contributors

Localised X-mode Reflectometry Measurements of Alfvén Eigenmodes on the JET Tokamak

Localised X-mode Reflectometry Measurements of Alfvén Eigenmodes on the JET Tokamak

S. Hacquin[1,5], S. E. Sharapov[2], B. Alper[2], C. Challis[2], A. Fonseca[1], E. Mazzucato[3], A. Meigs[2], L. Meneses[1], I. Nunes[1], S. D. Pinches[4,2] and JET EFDA contributors*

[1]*Associação EURATOM / IST, Centro de Fusão Nuclear, Av. Rovisco Pais, 1049-001 Lisbon, Portugal*
[2]*EURATOM/UKAEA Fusion Association, Culham Science Centre, OX14 3DB, UK.*
[3]*Princeton Plasma Physics Laboratory, James Forrestal Campus, Princeton, NJ08543, New Jersey, USA.*
[4]*Max-Planck-Institut für Plasmaphysik, EURATOM-Assoziation, D-85748 Garching, Germany.*
[5]*Association EURATOM / CEA, Centre de Cadarache, 13108 Saint-Paul lez Durance, France*
** See annex of J. Pamela et al, "Overview of JET Results ", (Proc. 20th IAEA Fusion Energy Conference, Vilamoura, Portugal (2004)).*

Preprint of Paper to be submitted for publication in
Plasma Physics and Controlled Fusion

ABSTRACT

The detection of Alfvén cascades is of great importance for the development of advanced plasma scenarios with reversed magnetic shear on the JET tokamak, since they allow the determination of the minimum of the safety factor. X-mode reflectometry is particularly powerful for this diagnosis since both the time-frequency evolution and the radial localisation of these Alfvén Eigenmodes (AEs) can be simultaneously obtained. This paper reports on the first successful localised measurements of AEs achieved with the recently upgraded X-mode reflectometry diagnostic on JET.

I. INTRODUCTION

The exploitation of Alfvén Eigenmodes (AEs) in advanced plasma scenarios with reversed magnetic shear and Internal Transport Barrier (ITB) has motivated an increasing interest in their diagnosis in the recent years. A particular interest arises for a specific class of AEs, the so-called Alfvén Cascades (ACs) observed in various tokamaks [1-4], due to their use in diagnosing the minimum of the safety factor, q_{min}. An accurate knowledge of q_{min} has proved to be especially valuable for the triggering of Internal Transport Barriers (ITBs) at low additional heating power [5-7]. Since the presence of AEs usually induces fluctuations of the magnetic field, the plasma density and the plasma temperature, various diagnostics – such as external magnetic pick-up coils, ECE radiometry and O-mode interferometry - have been used for their detection on JET. It has been shown in recent works [8, 9] that O-mode interferometry is one of the most powerful ways of determining the time-frequency evolution of AEs. Although such line-integrated measurements exhibit an unprecedented time and frequency resolution, they cannot provide direct radial localisation of the AEs. To overcome this limitation, X-mode reflectometry was demonstrated as a promising option [10, 11]. The first successful localised measurements of AEs on JET achieved with the recently upgraded X-mode reflectometry diagnostic are reported here. The paper is organised as follows; the theoretical principles required for the interpretation of X-mode reflectometry measurements are presented in Section 2. The application of X-mode reflectometry to localised measurement of AEs is discussed in Section 3. A brief presentation of the JET X-mode reflectometry diagnostic is given in Section III. The first experimental results of the localised measurements of AEs on the JET tokamak are presented and discussed in Section 4. Finally some conclusions are drawn in Section 5.

2. PRINCIPLES OF X-MODE REFLECTOMETRY MEASUREMENT

2.1. PHASE FLUCTUATIONS OF AN X-MODE REFLECTOMETER SIGNAL

An electromagnetic wave propagating in a magnetised plasma with X-mode polarisation (i.e. with its electric field perpendicular to the applied magnetic field) is affected by both the electron density and the magnetic field. Under the cold plasma approximation, the X-mode refractive index for a wave with frequency f propagating along the direction R can be written as [12]:

$$N(f,R)=\sqrt{1-\frac{X(f,R)\times(1-X(f,R))}{1-X(f,R)-Y^2(f,R)}} \tag{1}$$

The functions $X(f,R)$ and $Y(f,R)$ are proportional to the radial profiles of electron density and of magnetic field respectively, and are defined as follows:

$$X(f,R)=\frac{f_{pe}^2(R)}{f^2}=n_e(R)\times\frac{e^2}{4\pi^2\varepsilon_0 m_e f^2} \quad \& \quad Y(f,R)=\frac{f_{ce}(R)}{f}=B(R)\times\frac{e}{2\pi\, m_e f} \tag{2}$$

where f_{pe}, f_{ce}, e, m_e and ε_0 represent the electron plasma frequency, the electron cyclotron frequency, the electron charge, the electron mass and the vacuum permitivity. The wave is reflected by the plasma if it reaches a so-called cut-off layer where the refractive index drops to zero. From equations (1) and (2), it can be deduced that the X-mode has two distinct cut-off frequencies:

$$f_{cut-off}^{\pm}=\frac{1}{2}\left[\pm f_{ce}(R_c)+\sqrt{f_{ce}^2(R_c)+4f_{pe}^2(R_c)}\right] \tag{3}$$

where R_c indicates the cut-off layer position. An X-mode reflectometry diagnostic usually probes the plasma in the radial direction with a wave reflected by the upper branch (+ sign in equation (3)). Density fluctuations can then be inferred from the measurement of the phase perturbations of the reflected signal. In the case of smooth and stationary profiles of plasma density and magnetic field, the refractive index varies slowly over a wavelength so that the phase shift of the probing wave can be determined using the WKB approximation. Although the WKB approximation fails in the vicinity of the cut-off layer region, it can still be used to evaluate precisely the phase shift of a reflectometer probing wave after its round trip between the emitting/receiving antenna located at $R = R_{ant}$ and the cut-off layer at $R = R_c$ [13]:

$$\varphi(f)=2\times\frac{2\pi f}{c}\int_{R_{ant}}^{R_c(f)}N(f,R)\,dR-\frac{\pi}{2} \tag{4}$$

The initial factor of two accounts for the round trip of the wave, the $-\pi/2$ term illustrates the reflection at the cut-off layer and c is the light velocity in vacuum. Equation (4) remains valid even in the presence of plasma density fluctuations with a large radial envelope and small amplitude. Using the variables X and Y, the exact WKB solution for the phase fluctuations induced by such density fluctuations $\delta n_e(R)$ can then be written as:

$$\delta\varphi(f)=2\times\frac{2\pi f}{c}\int_{R_{ant}}^{R_c(f)+\delta R_c(f)}N(X+\delta X,Y)\,dR-\int_{R_{ant}}^{R_c(f)}N(X,Y)\,dR \tag{5}$$

where $\delta R_c(f)$ represents the oscillation of the cut-off layer and δX is derived from (2):

$$\delta X(f,R)=\delta n_e(R)\times\frac{e^2}{4\pi^2\varepsilon_0 m_e f^2} \tag{6}$$

Defining the variation of the refractive index along the line-of-sight:

$$\delta N(X,Y) = N(X+\delta X,Y) - N(X,Y) \tag{7}$$

equation (5) becomes:

$$\delta\varphi(f) = 2 \times \frac{2\pi f}{c}\left[\int_{R_{ant}}^{R_c(f)} \delta N(X,Y)\ dR + \int_{R_c(f)}^{R_c(f)+\delta R_c(f)} N(X+\delta X,Y)\, dR\right] \tag{8}$$

Considering small amplitude density fluctuations, the second integral in (8) accounting for the displacement of the cut-off layer can be neglected. Moreover we can assume that the refractive index variation given by (7) varies linearly with the amplitude of the density fluctuations, thus leading to:

$$\delta N(X,Y) = \delta X \times \frac{\partial N(X,Y)}{\partial X} + O(\delta X^2) \tag{9}$$

Finally, equations (6) and (1) are used to get a linear approximation of equation (8) [14]:

$$\delta\varphi_{approx}(f) = \int_{R_{ant}}^{R_c(f)} \delta n_e(R) \times G(f,R)\ dR \tag{10}$$

where the function $G(f,R)$ can be deduced from the radial profiles of plasma density and magnetic field:

$$G(f,R) = -\frac{e^2}{2\pi f \varepsilon_0 m_e c} \times \frac{(1-X(f,R))^2 + Y(f,R)^2 \times (2X(f,R)-1)}{(1-X(f,R)-Y(f,R)^2)^{3/2}\sqrt{(1-X(f,R))^2 - Y(f,R)^2}} \tag{11}$$

In this section, the linear expression (10) and the exact WKB expression (5) for the phase fluctuations are compared to assess the domain of validity of the linear approximation. As depicted in Figure 1, we used the following radial profiles of plasma density and magnetic field in our computations:

$$n_e(R) = n_0\left[1 - \left|\frac{R-R_0}{a}\right|^{\alpha}\right]^{\beta} \quad \& \quad B(R) = \frac{B_0 R_0}{R} \tag{12}$$

with typical JET parameters $n_0 = 3 \times 10^{19}$ m^{-3}, $a = 1$m, $\alpha = 2$, $\beta = 1$, $B_0 = 2.7$T and $R_0 = 3$m. Density fluctuations modelled by a Gaussian envelope located at $R_f = 3.4$ m were added to the unperturbed density profile defined by equation (12):

$$\frac{\delta n_e(R)}{n_0} = a_f\ exp\left[-\left(\frac{R-R_f}{W_f}\right)^2\right] \tag{13}$$

where their amplitude a_f was normalised to the density maximum n_0 and their width W_f was set to

various values. The displacement of the cut-off layer δR_c with respect to the probing frequency (deduced from the condition $N(X+\delta X,Y) = 0$) is shown in Figure 2 for $a_f = 2$ % and $W_f = 5$cm. A cut-off layer movement by more than 1 cm occurs for frequencies around 90GHz, which are reflected in the region of the density fluctuations. In Figure 3, the unperturbed and perturbed refractive index $N(X,Y)$ and $N(X+\delta X,Y)$ are compared for $f = 90$GHz, thus showing the clear displacement of the cut-off layer. As expected, the linear approximation for the refractive index variation fails in this case as confirmed by the discrepancies between expressions (7) and (9) shown in Figure 3. The phase fluctuations with respect to the probing frequency are depicted in Figure 4, showing that the discrepancies between expressions (5) and (10) can reach 15 % for the input parameters ($a_f = 2$ % and $W_f = 5$cm). Keeping the width of the density fluctuations equal to 5 cm, the precision of the linear approximation (10) is assessed as a function of the amplitude of the density fluctuations. As shown in Figure 5, the precision of the linear approximation is better than 10 % for density fluctuations with an amplitude up to 1%. Similarly, the effect of the width of density fluctuations with fixed amplitude of 1% is illustrated in Figure 6. The error using the linear expression remains below 10% as long as the width of the density fluctuations is larger than 3 cm. In conclusion, the linear expression (10) allows a good determination of the phase fluctuations of a reflectometer signal induced by density fluctuations with a large Gaussian envelope ($W_f > 3$ cm) and small amplitude ($a_f < 1$%).

2.2. EFFECT OF TRANSVERSE DENSITY FLUCTUATIONS ON THE PHASE RESPONSE

The results discussed in the previous section were obtained in a one-dimensional approach, thus neglecting the diffraction and interference phenomena induced by the finite apertures of the emitting and receiving antennas and by the finite width of the density fluctuations in the transverse directions. In large tokamaks like JET, the density fluctuations generally have a wide envelope in the toroidal direction so that our study was limited to the effect of the poloidal envelope of the density fluctuations.

To carry out computations in the poloidal section of a tokamak, the 2D computational method developed in previous works [9,14] was used. In this method it is assumed that the probing beam is composed of various independent rays defined by a poloidal wave-number k_Z. The weight of each ray is deduced from the spectrum of the emitting electric field E_0 in the plane ($R = R_{ant}$, Z) of the emitting and receiving antennas:

$$S(k_Z) = \int_{-\infty}^{+\infty} E_0(R = R_{ant}, Z)\, exp(-ik_Z Z)\; dZ \tag{14}$$

Then an inverse Fourier transform leads to the electric field reflected in the antenna plane ($R =$‘R_{ant}, Z) after propagation in the plasma:

$$E_{ref}(R = R_{ant}, Z) = \frac{1}{2\pi}\int_{-\infty}^{+\infty} S_Z(k_Z)\, exp(-i\varphi(k_Z))\; dZ \tag{15}$$

where the phase shift, φ for each probing ray labelled (k_y, k_z) is defined as:

$$\varphi(k_Z) = 2 \times \frac{2\pi f}{c} \int_{R_{ant}}^{R_c(k_Z)} \sqrt{N^2(f,R) - \left(\frac{k_Z c}{2\pi f}\right)^2}\, dR \; + k_Z Z - \frac{\pi}{2} + \delta\varphi(k_Z) \tag{16}$$

The three first terms in (16) represent the unperturbed phase and can be seen as a generalisation of equation (4) for oblique rays (k_Z•‘ 0). The last term corresponds to the phase fluctuations along the unperturbed ray trajectory and can be expressed as a generalisation of equation (10):

$$\delta\varphi(k_Z) = \int_{R_{ant}}^{R_c(k_Z)} \left[\frac{\delta n_e(R, Z^+(R)) + \delta n_e(R, Z^-(R))}{2}\right] \times G(f,R)\; dR \tag{17}$$

where $Z^+(R)$ and $Z^-(R)$ indicate the ray trajectory before and after reflection at the cut-off layer respectively, and the function $G(f, R)$ is defined by expression (11).

The received intensity in the antenna plane ($R = R_{ant}$, Z) is then given by:

$$I(Z) = E_{ref}(R = R_{ant}, Z) \times E_1(R = R_{ant}, Z) \tag{18}$$

where E_1 is the electric field that would be emitted by the receiving antenna.

Finally, we can define the following 1D and 2D expressions for the phase fluctuations:

$$\delta\varphi_{1D} = \delta\varphi(k_Z = 0) \tag{19}$$

$$\delta\varphi_{2D} = \frac{\int_{-\infty}^{+\infty} I(Z)\,\delta\varphi(k_Z(Z))\, dZ}{\int_{-\infty}^{+\infty} I(Z)\; dZ} \tag{20}$$

It can easily be noticed that expression (19) is equivalent to (10) and that the $d\varphi(k_Z(Z))$ term used in (20) is deduced from equation (17) and from the k_Z ray trajectory. To assess the contribution of poloidal density fluctuations from expression (20), the determination of the ray trajectory is required to compute expressions (15-18). Assuming a slab model (i.e. neglecting the curvature of the magnetic surfaces, which is a good assumption in the JET mid-plane plasma probed by the X-mode reflectometer) and constant plasma density and magnetic field in the poloidal direction (i.e. $N(R,Z) = N(R)$), the poloidal wave-number k_Z remains constant along the ray trajectory, which is defined by [12]:

$$\frac{dR}{d\tau} = \frac{\partial N(f, k_R, k_Z)}{\partial k_R} \quad \& \quad \frac{dZ}{d\tau} = \frac{\partial N(f, k_R, k_Z)}{\partial k_Z} \tag{21}$$

with the refractive index given by:

$$N(f, k_R, k_Z) = \frac{c}{2\pi f}\sqrt{k_R^2 + k_Z^2} \tag{22}$$

The equation of the ray trajectory can be derived from expressions (21) and (22):

$$\frac{dZ}{dR} = \pm \frac{1}{\sqrt{\left(\frac{2\pi f N(R)}{k_Z c}\right)^2 - 1}} \tag{23}$$

where the sign ± indicates the propagation before and after reflection by the plasma.

In order to solve analytically equation (23), we assume in the following that the square of the refractive index has a parabolic shape between the antenna position R_{ant} and the cut-off layer postion R_c:

$$N^2(R) = a(R - R_{ant})^2 + b(R - R_{ant}) + c \tag{24}$$

By definition, the parameter $c = 1$ since the antenna is located in the vacuum and $N^2(R = R_{ant}) = 1$. Moreover, the condition $\frac{\partial N^2(R = R_{ant})}{\partial R^2} = 0$ ensures a smooth vacuum-plasma transition, thus leading to $b = 0$. Considering that $N^2(R = R_c(k_Z = 0)) = 0$ for the normal ray of the probing beam, the parameters are finally given by:

$$a = \frac{-1}{(R_c(k_Z = 0) - R_{ant})^2}; \qquad b = 0; \qquad c = 1 \tag{25}$$

It can be noticed that a is negative, which is physically consistent. Under these hypotheses, equation (23) can be solved analytically to give explicit expressions for the ray trajectory, before and after reflection at the cut-off layer position:

$$Z^+(R) = Z(R_{ant}) + \frac{sign(k_Z)}{\sqrt{-a}} \times arctan\left(\frac{\sqrt{-a}(R - R_{ant})}{\sqrt{\left(\frac{2\pi f N(R)}{k_Z c}\right)^2 - 1}}\right) \tag{26}$$

$$Z^-(R) = Z_c(k_Z) + \frac{sign(k_Z)}{\sqrt{-a}} \times \left[arctan\left(\frac{\sqrt{-a}(R - R_{ant})}{\sqrt{\left(\frac{2\pi f N(R)}{k_Z c}\right)^2 - 1}}\right) + \frac{\pi}{2}\right] \tag{27}$$

The position of the cut-off layer can be deduced from the cut-off condition $N(R_c) = \frac{k_Z c}{2\pi f}$ and equations (24-27):

$$R_c(k_Z) = R_{ant} - \frac{\sqrt{1 - \left(\frac{k_Z c}{2\pi f}\right)^2}}{\sqrt{-a}} \tag{28}$$

$$Z_c(k_Z) = Z^-(R_c(k_Z)) = Z^+(R_c(k_Z)) = Z(R_{ant}) - \frac{sign(k_Z)}{\sqrt{-a}} \times \frac{\pi}{2} \tag{29}$$

The functions $X(f,R)$ and $Y(f,R)$ defined by (2) should be chosen in order to satisfy equations (24-25) of a parabolic shape for the square of the refractive index. Combining equation (1) and equation (24) with a, b and c defined by (25), we obtain:

$$X(f,R) = \frac{1 - a(R - R_{ant})^2 \pm \sqrt{\left(1 - a(R - R_{ant})^2\right)^2 + 4a\,(R - R_{ant})^2 (1 - Y(f,R)^2)}}{2} \tag{30}$$

where the signs + and – correspond to the lower and the upper branches respectively. In the computations presented here, $Y(f,R)$ was defined by equations (2) and (12) with B_0 = 2.7T and R_0 = 3m and in turn $X(f,R)$ was determined from expression (30). As depicted in Figure 7, the cut-off layer is located at R = 3.2m for a probing frequency of 100GHz. The ray tracing determined from equations (26-27) is illustrated in Figure 8. The following density fluctuations in both the radial and the poloidal directions were located in the cut-off layer region:

$$\frac{\delta n_e(R,Z)}{n_0} = a_f \, exp\left[-\left(\frac{R - R_f}{Wr_f} \right)^2 \right] \times \left[cos\left(\frac{\pi}{2} \times \frac{Z - Z_f}{Wz_f} \right) \right]^2 \tag{31}$$

with the settings $n_0 = \max(n_e)$, a_f = 0.5 %, $R_f = R_c(k_z = 0)$, Wr_f = 6 cm, $Z_f = Z_{ant}$. The last parameter Wz_f was changed to study the influence of the width of the poloidal density fluctuations. Note that the position and aperture of the receiving and emitting antennas were set to match the JET X-mode reflectometer characteristics in the computations of expressions (19) and (20). As an illustration of the effect of the poloidal density fluctuations, the phase fluctuations (17) together with the received intensity (18) in the antenna plane $R = R_{ant}$ (used in the calculation of expression (20)) are exemplified in Figure 9 for Wz_f = 10 cm. The discrepancies between 1D and 2D computations were then inferred from comparison of expressions (19) and (20) for various widths of poloidal density fluctuations. Since the distance between the emitting/receiving antennas and the reflecting layer is also expected to play an important role, the computations were carried out for several distances $|R_{ant} - R_c|$. The results obtained for 2.5 cm < Wz_f < 50 cm and for $|R_{ant} - R_c|$ = 20, 50 and 80 cm are presented in Figure 10. In the advanced scenarios developed at JET, Alfvén Eigenmodes are usually observed at R < 3.5m, which means at least 50cm away from the antennas. It is noticeable that in this case the 1D approximation remains accurate to within 10 % for widths of the poloidal density fluctuations larger than 3-4cm. In other words, the 1D expression (10) for the phase fluctuations of a reflectometer signal in the presence of Alfvén Eigenmodes can be used as long as the following relation is satisfied:

$$2\,Wr_f = \frac{2\pi \left| R_{AE} - R_{axis} \right|}{m} > 8\,cm \tag{32}$$

where R_{AE}, R_{axis} and m are the radial location of the Alfvén Eigenmodes (AEs), the magnetic axis and the poloidal mode number of the AEs. On JET, $|R_{AE} - R_{axis}|$ is on the order of magnitude of 20-30cm indicating that 1D expression (10) reliably reproduces the phase fluctuations induced by density fluctuations with poloidal mode number up to $m = 20$. Let us note that all the tools developed in section II to evaluate the phase fluctuations of a reflectometer signal can easily be applied to the case of O-mode reflectometry by simply setting $Y(f,R) = 0$ in all the previous expressions.

3. LOCALISED X-MODE REFLECTOMETRY MEASUREMENTS OF ALFVÉN EIGENMODES

3.1. MEASUREMENT OF DENSITY FLUCTUATIONS USING X-MODE REFLECTOMETRY

In this section how the density fluctuations associated with Alfvén Eigenmodes (AEs) can be inferred from the phase fluctuations of an X-mode reflectometer is discussed. It was shown in the last section that in large tokamaks like JET, the phase fluctuations of a reflectometer signal were generated mainly by radial density fluctuations. For Alfvén Cascades with radial mode $l = 0$ for instance [15], the associated density fluctuations can be modelled by:

$$\delta n_e(R) = a_{LFS}\, exp\left[-\left(\frac{R - R_{LFS}}{W_{LFS}}\right)^2\right] + a_{HFS}\, exp\left[-\left(\frac{R - R_{HFS}}{W_{HFS}}\right)^2\right] \tag{33}$$

Equation (33) is in agreement with the localisation of the density fluctuations in both the Low-Field-Side (LFS) and the High-Field-Side (HFS) regions, as expected by magnetic equilibrium codes [16,17]. The phase fluctuations of a X-mode reflectometer signal can then be deduced from expression (10). As illustrated in Figure 11, the electron density and the magnetic field in JET advanced scenarios can be defined by equations (12) with typical JET parameters $n_0 = 4 \times 10^{19}$ m^{-3}, $a = 1$m, $\alpha = 4$, $\beta = 1$, $B_0 = 2.7$T and $R_0 = 3$m. The phase fluctuations with respect to the probing frequency are exemplified in Figure 12. From the radial profile of the upper cut-off layer given by (3) and represented in Figure 11, a cut-off layer position can be associated with each probing frequency (as illustrated in Figure 12). Then the phase fluctuations of a reflectometer signal can be defined with respect to the radial position of the cut-off layer. Figure 13 shows the radial profile of phase fluctuations in the presence of density fluctuations defined by (33) with $a_{LFS} = 0.2$ %, $R_{LFS} = 3.3$m, $W_{LFS} = 5$cm, $a_{HFS} = 0.5$ %, $R_{HFS} = 2.7$m and $W_{HFS} = 6$cm. It is noticeable from Figure 13 that the phase response is clearly localised in the density fluctuation regions. This shows the capability of X-mode reflectometry for localised measurement of density fluctuations, even in flat density profile regions where localised measurements from O-mode reflectometry are not possible (as discussed in [9]). As done for density profile reconstruction [18], an inversion technique could be used to determine the radial profile of density fluctuations from the radial profile of phase fluctuations given by an X-mode reflectometer. However, a good spatial resolution for the profile of phase

fluctuations would be needed, which requires a large number of probing channels in the desired frequency range. In practice the majority of the fluctuation reflectometers only use a few frequency channels, thus making such a technique too difficult and inaccurate. Alternatively, a minimising procedure can be used. Assuming that the phase fluctuations of probing waves reflected at different radial positions satisfy equation (10) and that the density fluctuations associated with AEs have a radial envelope given by equation (33), the characteristics of the density fluctuations a_f, R_f and W_f (either at the LFS or at the HFS) can be deduced from:

$$\mathrm{Min}\left[\sum_{i=1}^{n}\left(\delta\varphi(R_i) - a_f \times n_0 \times \int_{R_{ant}}^{R_i} \exp\left[-\left(\frac{R - R_f}{W_f}\right)^2\right] \times G(f,R)\ dR\right)^2\right] \qquad (34)$$

where $d\varphi(R_i)$ are n experimental measurements of phase fluctuations. Note that the normalisation density factor n_0 (which can be either the maximum density or the local density at $R = R_f$) and the function $G(f,R)$ defined by expression (11) are estimated from the radial profiles of plasma density and magnetic field. Equation (34) has to be used separately to determine the density fluctuations in the LFS region and in the HFS region. Therefore, the radial separation between the density fluctuations in the LFS and the HFS regions have to be large enough so that the phase fluctuations coming from these two distinct regions do not overlap. In Figure 13 where the density fluctuations in the LFS and HFS regions are separated by 60cm, it can be noticed that the phase fluctuations in the HFS region is still slightly affected by the density fluctuations localised in the LFS region. In this case, some simulations have pointed out that the number n of experimental measurements should be high enough in order to ensure a good determination of the density fluctuation characteristics. Finally, it was found that at least three experimental measurements within the density fluctuation region ($n \geq 3$) are required for a precise measurement. There are two ways of obtaining enough experimental points to reconstruct the density fluctuations from equation (34). The most obvious one is to have enough probing frequency channels, which is not always the case as the number of channels is generally fixed by the hardware characteristics of the reflectometer diagnostic. Another option is to change the plasma parameters (for instance by sweeping the magnetic field value or by increasing the density with additional heating) in order to move the positions of the cut-off layers of the probing frequency channels. However, it must be assumed that the density fluctuations remain the same for a reliable use of expression (34).

3.2. THE JET X-MODE REFLECTOMETRY DIAGNOSTIC

The JET X-mode reflectometry diagnostic is composed of four distinct radial correlation reflectometers. All these reflectometers probe the mid-plane JET plasma with two distinct waves - one at fixed frequency (76, 85, 92 and 103GHz respectively) and the other at a tuneable frequency (in the 76-78, 85-87, 92-96 and 100-106GHz frequency band respectively) - to allow radial correlation measurements. All the frequency channels are equipped with I/Q detectors so that the phase

fluctuations from all these channels can be measured. The entire diagnostic is controlled remotely by a VME-PC system via an Ethernet connection. More details on the characteristics of the JET X-mode reflectometer system can be found in [19, 20]. The performance of this system has been significantly improved with new low-attenuation transmission lines installed under the EFDA enhancement project "Millimetre Wave Access" [21]. Measurements of density fluctuations localised in the plasma core region are now possible [22]. For the measurements of density fluctuations associated with Alfvén Eigenmodes reported in this paper, all the frequencies of the tuneable channels were kept constant so that the diagnostic was used as a multi-channel reflectometer system. An example of the radial profile of upper cut-off frequency (determined from the density profile measured by the JET LIDAR Thomson scattering diagnostic [23] and from the magnetic field profile given by the EFIT equilibrium code [24]) for a typical magnetic reversed-shear JET discharge at 2.4T is depicted in Figure 14, thus illustrating that the various frequency channels of the JET X-mode reflectometer probe different radial positions in the plasma. In particular the core and high-field-side regions not accessible with the O-mode, can be probed with the X-mode [25]. The cut-off layer positions for the various probing frequencies depend on both the plasma density profile and the magnetic field profile for the X-mode. In this particular situation, it is noticeable that the channels of the X-mode reflectometer diagnostic (only channels at frequencies 78, 85, 92 and 103GHz are represented in Figure 14) can be either in the reflectometry regime (reflected by the plasma) or in the interferometry regime (reflected by the inner wall). Similar to previous works using O-mode interferometry measurements [8, 9], it was checked that X-mode interferometry measurements could also be used to determine the time-frequency evolution of AEs. Nonetheless, the interest in using X-mode polarisation is to localise these modes, which requires reflectometry measurements. In the next section the first localised measurements of AEs on JET achieved using X-mode reflectometry are presented.

4. EXPERIMENTAL RESULTS

A dedicated experimental session was held at JET to optimise the plasma conditions for X-mode reflectometry measurements of AEs. A set of reversed shear discharges with different applied magnetic fields and additional heating schemes was successfully carried out. The results obtained for the JET Pulse No: 66529 performed at a magnetic field of 2.9T, which was found to be a good compromise for optimising the X-mode reflectometry measurements of AEs, are presented in this section. Presented in Figure 15 are the cut-off layer positions for various X-mode reflectometer channels, thus showing that a good coverage of the JET plasma radius is achieved at this magnetic field. Some NBI heating is applied up to t = 6s, and a smooth decrease of the plasma density after the NBI power is switched off at t = 6s can be seen in Figure 15. As expected, the cut-off layers of the various X-mode reflectometer channels move inwards in the plasma as the average density decreases, allowing a wider radial coverage of the probed zones. Taking advantage of the I/Q detection, the phase perturbations from each frequency channel can then be computed. The

spectrograms (computed from a sliding FFT technique) of the phase perturbations from the 85GHz and 103GHz channels are depicted in Figure 16 (for clarity of the AEs picture, phase perturbations only up to 0.25 radians were represented). Before t = 6.5s, some Toroidal Alfvén Eigenmodes (TAEs) are observed around 180kHz on the 85GHz channel. From the same channel, it can be noticed that the TAEs become less clear after t = 6.5s while in the meantime some Alfvén Cascades (ACs) appear. This suggests that the TAEs and the ACs are located at slightly different radial positions. After t = 6.5s, some ACs appear on both the 85GHz and the 103GHz channels, whose cut-off layers are localised at $R \cong 3.35$m and $R \cong 2.6$m respectively. The ACs are not observed before t = 6.5s, because the density is higher and the cut-off layers are localised further out in the plasma at $R \geq 3.35$m and $R \geq 2.8$m (for the 85GHz and the 103 GHz channels respectively). This clearly indicates that the ACs are strongly localised at two distinct radial positions, namely in the low field side (LFS) and High Field Side (HFS) regions. A cut at t = 6.87s of the phase perturbations from all channels is shown in Figure 17. A strong peak with phase perturbations of almost 1 radian for f = 85kHz is observed in the two higher frequency signals, which are reflected in the HFS region at $R \cong 2.6$m. Another peak with smaller amplitude of 0.3 radian for the same frequency f = 85kHz is also observed on the 85GHz signal, which is reflected in the LFS region at $R \cong 3.35$m. Figure 17 clearly shows that not only the frequency of an AE, but also its radial location can be inferred from a multi-channel X-mode reflectometer. A statistical estimation of the level of phase perturbations induced by ACs has been carried out over a half a second time window. Since the respective cut-off layers of the various reflectometry channels move within this time window due to density profile changes, the distribution of phase perturbations as a function of the plasma major radius can be inferred (see Fig.18). Two peaks of phase perturbations, one smaller in the low-field-side region at $R \cong 3.35$m and another higher in the high-field-side region at $R \cong 2.6$m, are clearly noticeable. The position of these peaks is in good agreement with the position of the minima of the safety factor q_{min}, thus confirming that ACs are localised in these regions. These results also confirm theoretical estimations of the radial shape of the density fluctuations associated with Alfvén cascades based on equilibrium reconstruction and MISHKA and NOVA-K simulations [3]. Considering from Figure 18 the maximum of the phase fluctuations with respect to the major radius $dj(R)$, an estimation of the density fluctuation characteristics can be inferred. Assuming that the density fluctuations remain roughly constant during the change of plasma density, enough experimental measures within the density fluctuation regions are available for estimation of equation (34). To match the phase fluctuations obtained experimentally, we calculated normalised density fluctuations of 5×10^{-4} and a width of 6cm in the HFS region (at R = 2.6m) and normalised density fluctuations of 2×10^{-4} and a width of 5cm in the LFS region (at R = 3.35m).

CONCLUSIONS

Diagnosis based on the excitation and observation of Alfvén Eigenmodes (AEs) such as Alfvén Cascades (ACs) has proved to be very useful for studying advanced plasma scenarios in tokamak

devices. The detection of ACs is for instance used for the determination of the safety factor minimum q_{min}, which is of the great importance for the development of advanced scenarios with Internal Transport Barriers (ITBs). Therefore a strong demand has recently appeared for reliable diagnostics allowing measurement of ACs with high resolution. It was show in previous works that O-mode reflectometry (used in the interferometry regime) has a good potential for determining the time evolution of q_{min} since it usually gives a better representation of the ACs than other diagnostics, such as the external magnetic pick-up coils. Although O-mode reflectometry and the magnetic pick-up coils are now routinely used for the time-frequency determination of Alfvén Eigenmodes, none of these diagnostics gives a direct radial localisation of such modes on JET. In addition to a clear time-frequency detection of the AEs, this paper demonstrates that X-mode reflectometry also allows radial localisation of these modes. The first localised measurements of AEs using X-mode reflectometry on JET reported in this paper are important for the development of advanced scenarios in tokamaks. In addition, these results are particularly relevant to ITER for the two following reasons. Firstly, magnetic pick-up coils will require special protection for the detection of AEs on ITER and secondly, JET is the only tokamak in the world offering challenging conditions close to those in which the reflectometry measurements will be performed on ITER (with for instance the use of up to eighty metres of transmission lines).

ACKNOWLEDGEMENTS

This work has been partly carried out in the frame of the Contract of Association between the European Atomic Energy Community and “Instituto Superior Técnico” (IST) and of the Contract of Associated Laboratory between “Fundação para a Ciência e Tecnologia” (FCT) and IST. The content of the publication is the sole responsibility of the authors and it does not necessarily represent the views of the Commission of the European Union or FCT or their services. The authors would like to thank Mike Bennett and John Fessey for technical assistance with the X-mode reflectometer acquisition system and Mike Walsh for encouragement in this work.

REFERENCES

[1]. Kimura H. *et al* 1998 *Nucl. Fusion* **38** 1303
[2]. Sharapov S.E. *et al* 2001 *Phys. Lett.* A **289** 127
[3]. Nazikian R. *et al* 2003 *Phys. Rev. Lett.* **91** 125003
[4]. Snipes J. *et al* 2005 *Phys. Plasmas* **12** 056102
[5]. Sharapov S.E. *et al* 2002 *Phys. Plasmas* **9** 2027
[6]. Joffrin E. *et al* 2002 *Plasma Phys. Control. Fusion* **44** 1739
[7]. Joffrin E. *et al* 2003 *Nucl. Fusion* **43** 1167
[8]. Sharapov S.E. *et al* 2004 *Phys. Rev. Lett.* **93** 165001
[9]. Hacquin S. *et al* 2006 *Nucl. Fusion* **46** S714
[10]. Nazikian R. *et al* 1997 *Phys. Rev. Lett.* **78** 2976

[11]. Hacquin S. *et al* 2006 *Proc. 33nd EPS Conf. on Plasma Physics and Controlled Fusion*
[12]. Swanson D.G. 2003 *Plasma Waves* 2nd ed. (Bristol: IOP Publishing Ltd)
[13]. Hutchinson I. 2002 Principles of Plasma Diagnostics 2nd ed. (Cambridge University Press)
[14]. Gusakov E. and Popov A. 2004 *Plasma Phys. Control. Fusion* **46** 1393
[15]. Breizman B. *et al* 2003 *Phys. Plasmas* **10** 3649
[16]. Sharapov S.E., Mikhailovskii A.B. and Huysmans G.T. 2004 *Phys. Plasmas* **11** 2286
[17]. Cheng C.Z. 1992 *Phys. Rep.* **211** 1
[18]. Clairet F. *et al* 2001 *Plasma Phys. Control. Fusion* **43** 429 & Bottollier-Curtet H. and Ichtchenko G. 1987 *Rev. Sci. Instrum.* **58** 539
[19]. Conway G. *et al* 1999 *Rev. Sci. Instrum.* **70** 3921
[20]. Hacquin S. *et al* 2004 *Rev. Sci. Instrum.* **75** (10) 3834
[21]. Cupido L. *et al* 2005 *Fusion Engineering and Design* **74** (1-4) 707
[22]. Hacquin S. *et al* 2006 *Rev. Sci. Instrum.* **77** 10E925
[23]. Gowers C. *et al* 1995 *Rev. Sci. Instrum.* **66** 471
[24]. O'Brien *D. et al* 1992 *Nucl. Fusion* **32** 1351
[25]. Mazzucato E. 1998 *Rev. Sci. Instrum.* **69** 1691

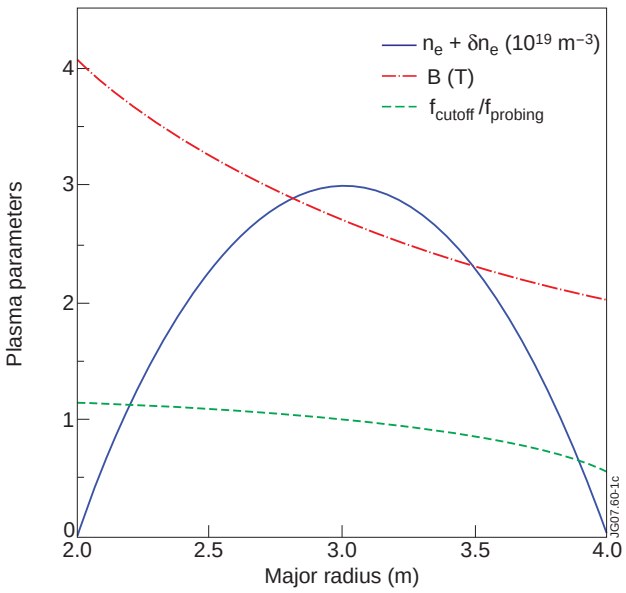

Figure 1: Radial profiles of density (full line), magnetic field (dash-dot line) and X-mode upper cut-off frequency (normalised to f = 100GHz in dashed line) used in 1D WKB simulations to assess the effect of density fluctuations on the phase of a reflectometer signal.

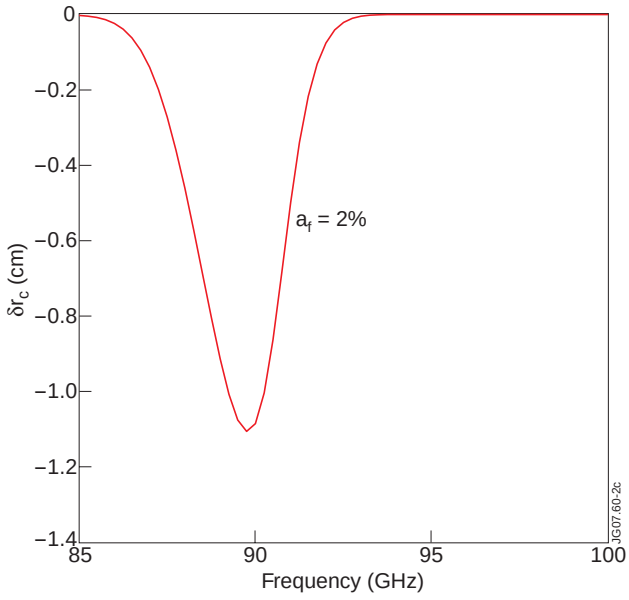

Figure 2: Cut-off layer displacement induced by a Gaussian density fluctuation (located at R = 3.4m with amplitude of 2 % and width of 5cm) with respect to the probing frequency.

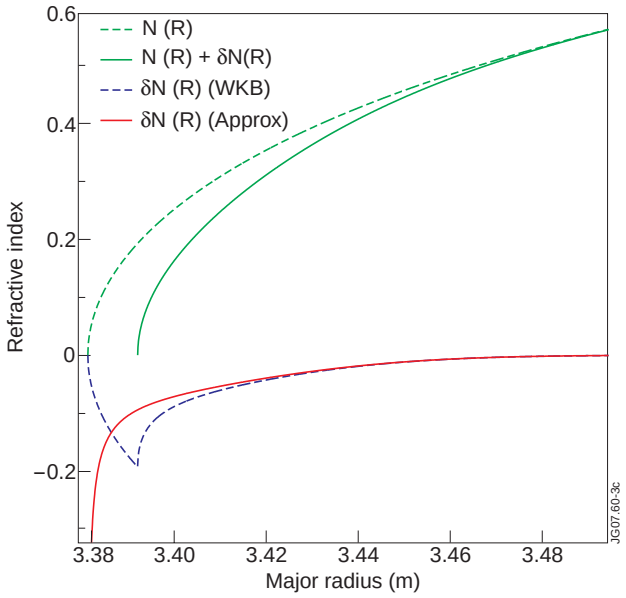

Figure 3: Linear approximation in the presence of a significant displacement of the cut-off layer (for f = 90GHz); in the positive part is represented the refractive index without (dashed line) and with (full line) fluctuations; in the negative part is shown the refractive index fluctuation (exact WKB solution in dashed line and linear approximation in full line).

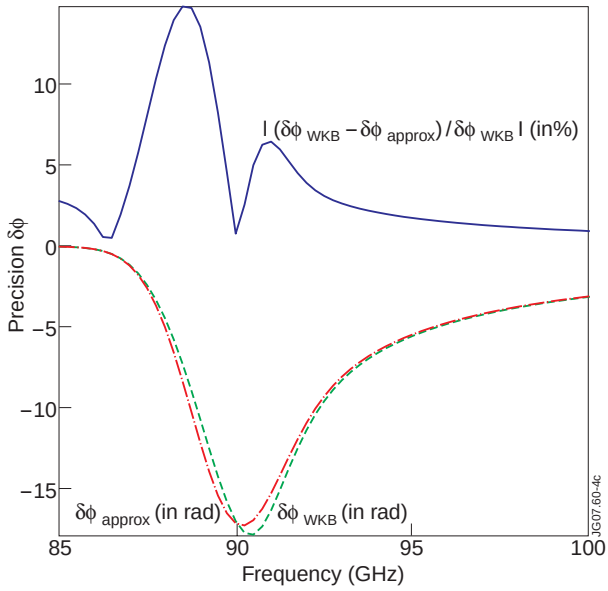

Figure 4: Phase fluctuation from WKB computation (dashed line), phase fluctuation from linear approximation (dash-dot line) and precision of the linear approximation (full line) as a function of the probing frequency.

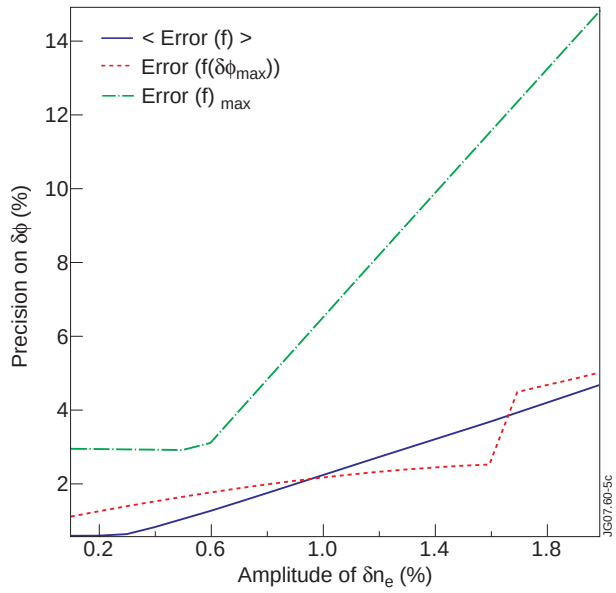

Figure 5: Precision of the linear approximation as a function of the amplitude of the density fluctuations (with width of 5cm): error averaged over various frequencies (full line), error for the frequency corresponding to the maximum phase fluctuation (dashed line) and maximum error (dash-dot line).

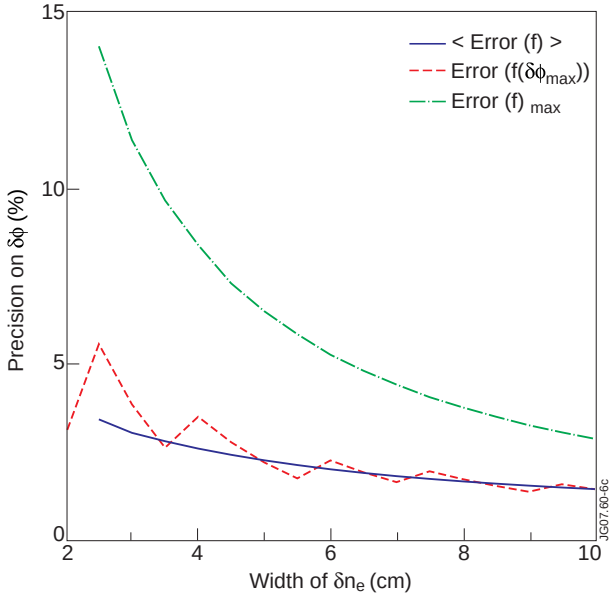

Figure 6: Precision of the linear approximation as a function of the width of the density fluctuations (with amplitude of 1%): error averaged over various frequencies (full line), error for the frequency corresponding to the maximum phase fluctuation (dashed line) and maximum error (dash-dot line).

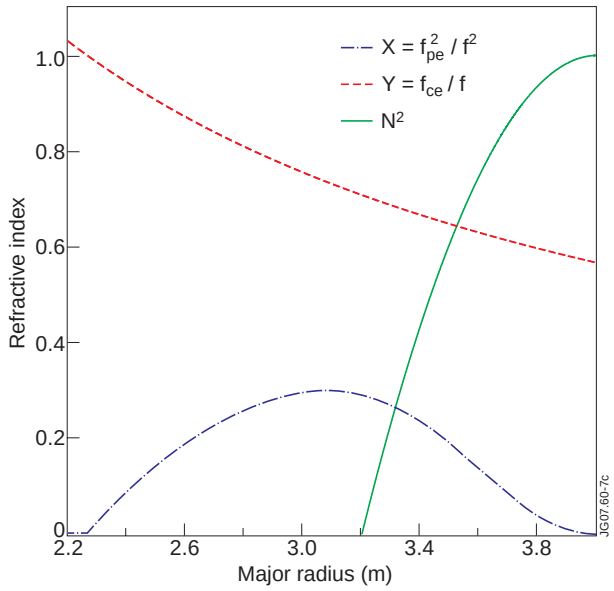

Figure 7: Parabolic radial profile of the square of the refractive index (full line), normalised density profile (function X in dash-dot line) and normalised magnetic field profile (function Y in dashed line) for a probing frequency f = 100GHz reflected at R = 3.2m.

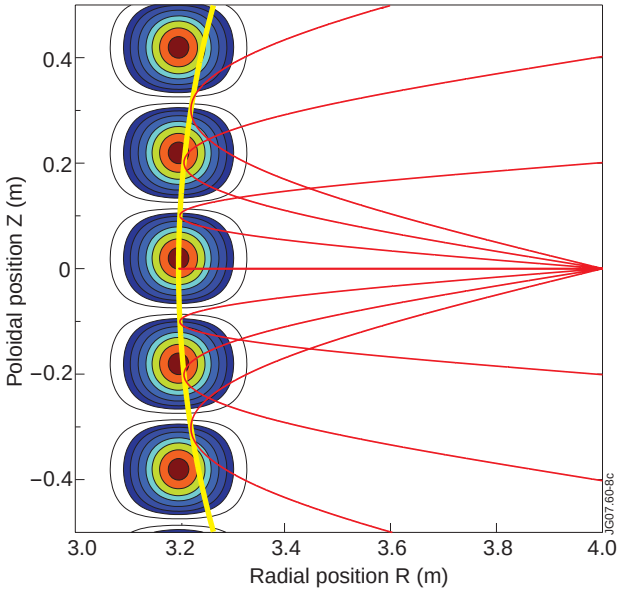

Figure 8: 2D ray-tracing simulations to investigate the effect of density fluctuations in the vicinity of the cut-off layer on the phase of a reflectometer signal.

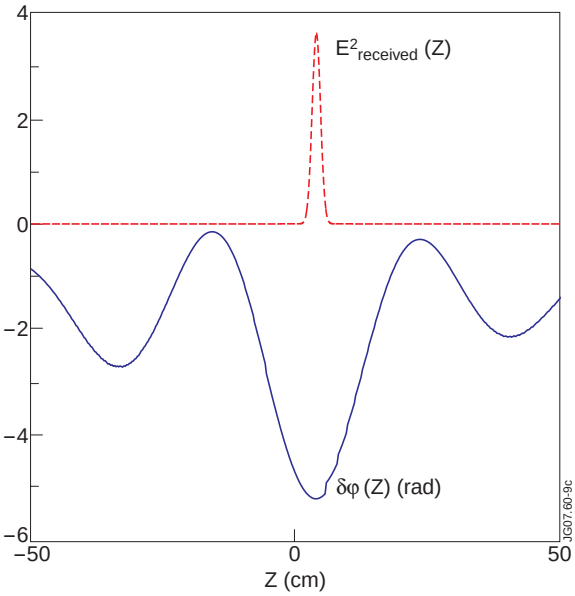

Figure 9: Effect of transverse density fluctuations on the phase of the reflected signal; phase fluctuations of the reflected signal and electric field of the received signal in the antenna plane (R = R_{ant}, Z).

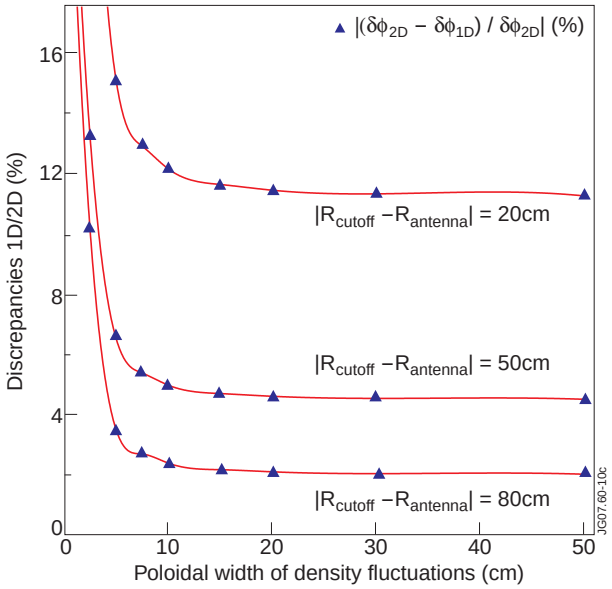

Figure 10: Discrepancies between 1D and 2D computations with respect to the transverse width of the density fluctuations for various distances between the emitting/receiving antennas and the cut-off layer position.

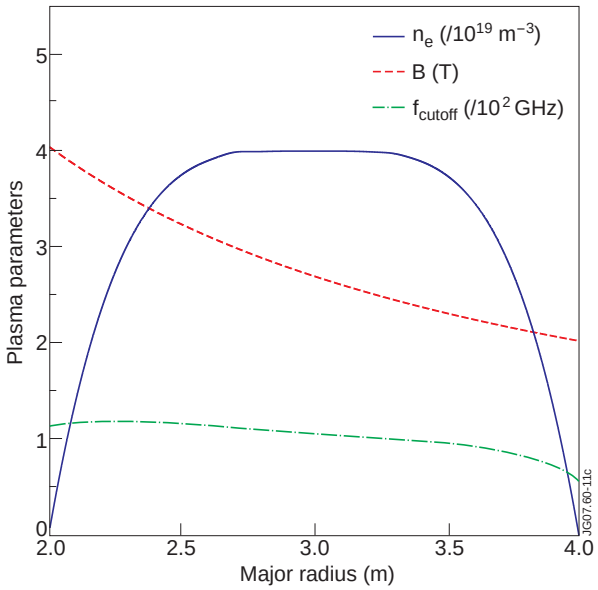

Figure 11: JET-like radial profiles of density (full line), magnetic field (dashed line) and X-mode upper cut-off frequency (dash-dot line) used in 1D WKB computations of the phase perturbations induced by density fluctuations associated with Alfvén Cascades.

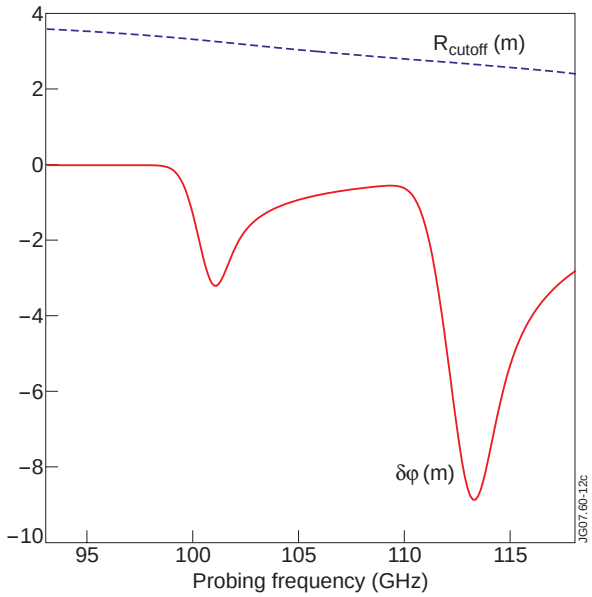

Figure 12: Phase perturbations induced by density fluctuations associated with Alfvén Cascades (full line) and radial position of the cut-off layer (dashed line) with respect to the probing frequency.

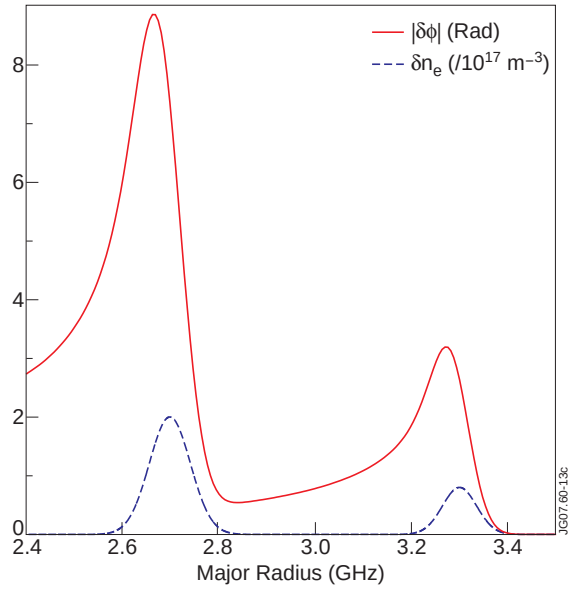

Figure 13: Absolute phase perturbations (full line) induced by density fluctuations associated with Alfvén Cascades (dashed line) with respect to the radial position.

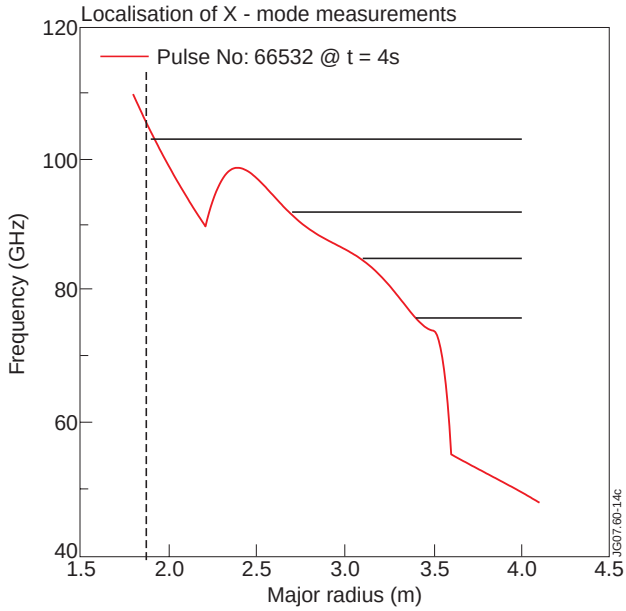

Figure 14: Example of radial profile of X-mode upper cut-off frequency (full line) for a typical JET discharge at 2.4T (the position of the inner wall is indicated by the dashed line). Four channels of the X-mode reflectometer are represented by the horizontal black lines.

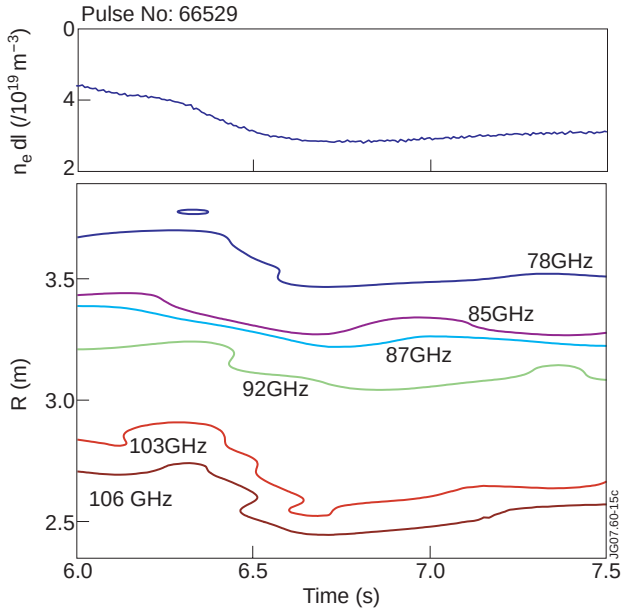

Figure 15: Line-integrated density measured with the JET FIR interferometer and cut-off layer positions (deduced from the density profile obtained with the JET Thomson scattering LIDAR diagnostic and from the magnetic field profile given by an EFIT equilibrium reconstruction) of different X-mode reflectometer channels.

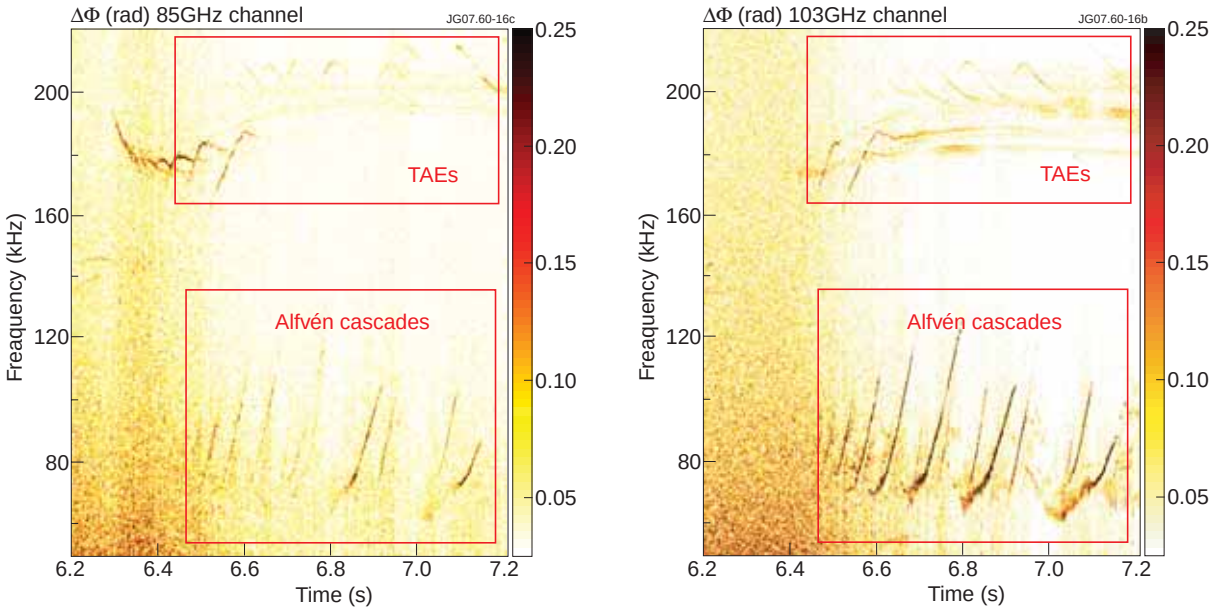

Figure 16: Spectrograms of the phase perturbations from the X-mode reflectometer 85GHz (right side) and 103GHz (left side) channels, probing the low field side and the high field side respectively (as shown on Figure 15).

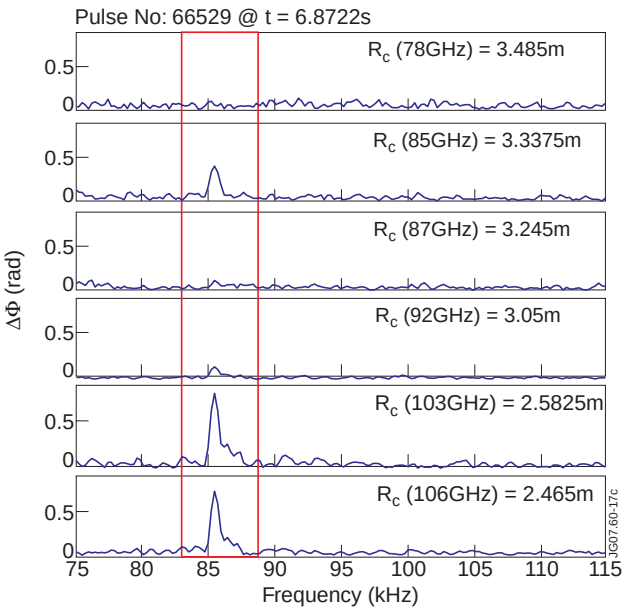

Figure 17: Phase perturbations from different X-mode reflectometry channels. The localisation of an Alfvén cascade with frequency of 85kHz can be deduced from the corresponding cut-off layer positions.

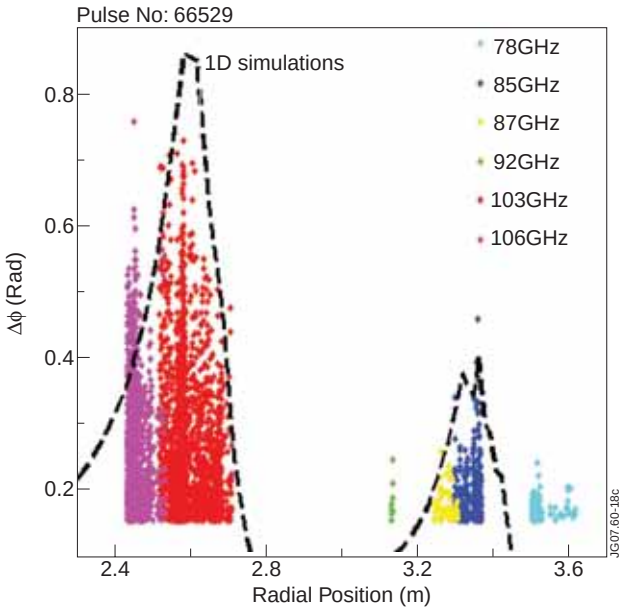

Figure 18: Statistical radial distribution (within a time-frequency window) of the phase perturbations induced by Alfvén cascades, displaying two clear peaks - one at the low-field-side and another with higher amplitude at the high-field-side.